CHEMISTRY OF MATERIALS
Cite This: Chem. Mater. 2019, 31, 7779−7789
Article
pubs.acs.org/cm

Single-Source Precursors for Lanthanide Diselenide Nanosheets

Rida Atif,[†] Aleksej Zarkov,[†,‡] Dane Romar C. Asuigui,[†] Priscilla Glaser,[†] Orlando Stewart, Jr.,[†] and Sarah L. Stoll*[,†]

[†]Department of Chemistry, Georgetown University, 37th and O Streets NW, Washington, D.C. 20057, United States
[‡]Institute of Chemistry, Vilnius University, Naugarduko 24, LT-03225 Vilnius, Lithuania

Supporting Information

ABSTRACT: A series of complexes of the type $[Ln(Se_2P(phenyl)_2)_3(CH_3CN)_x]$ (x = 1 or 2) have been synthesized and structurally characterized for Ln = La−Lu (excluding Pm). The complexes are straightforward to prepare and crystallize and are soluble in solvents typically used in nanoparticle synthesis. Solution-phase thermolysis of these complexes formed lanthanide diselenide or $LnSe_{2-x}$ nanosheets, for Ln = La−Ho, except Eu, which formed EuSe. By contrast, the smallest lanthanides Ln = Er−Lu formed Ln_2Se_3 nanomaterials. The lanthanide dichalcogenides are rare-earth analogues of the transition metal dichalcogenides and exhibit similar properties, including small band gaps, charge density waves, antiferromagnetism, and superconductivity. The lanthanide diselenide nanomaterials exhibited highly anisotropic growth and were phase pure with the exception of $CeSe_2$ (which also formed a cerium oxide and cerium ultraphosphate). The lateral nanosheet dimensions, based on transmission electron microscopy (TEM), range from ∼50 to 500 nm, and the thickness was found to be ∼4 nm for the thinnest sheets by atomic force microscopy. The nanosheets were further characterized by powder X-ray diffraction, scanning electron microscopy, and Raman spectroscopy. Alloy formation was also demonstrated with the combined solution thermolysis of Sm and Gd complexes to form $Sm_{1-x}Gd_xSe_{1.8}$. The alloy was found to have homogeneous composition on the basis of powder X-ray diffraction and TEM.

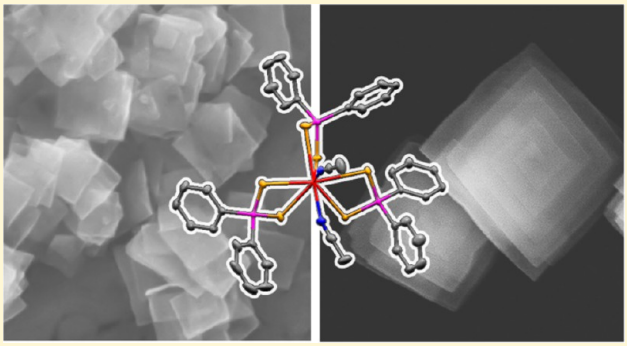

INTRODUCTION

Layered materials have long been studied for the novel properties that result from structural anisotropy,[1−3] and recently, excitement has been generated by the ability to prepare atomically thin nanosheets, termed "two-dimensional" materials.[4] Two-dimensional (2D) materials have attracted interest because of properties that differentiate them from the bulk,[5] as well as improved mechanical flexibility, and enhanced electrical and optoelectronic properties.[6−8] In addition to fundamental knowledge, there is the potential for a wide range of applications from batteries to photodetectors, thermoelectrics, catalysis,[9] and new device development.[10] Layered materials also open synthetic opportunities to tune properties through intercalation, exfoliation, reassembly of sheets of two different materials, or alloying within the layer.[11] Changes from direct to indirect band gaps as well as valley polarization have drawn significant attention to the transition metal dichalcogenides (TMDs).[12] Among new classes of 2D materials, there has been growing interest in 2D rare-earth nanomaterials[13] because of the novel luminescent, magnetic, and catalytic properties conferred by the nonbonding nature of the 4f electrons.[14]

The lanthanide dichalcogenides, LnX_{2-x} (Ln = lanthanide, and X = S, Se, or Te), are an underexplored class of rare-earth materials that form novel analogues of the TMDs, and the structures are compared in Figure 1. Like the TMDs, the LnX_{2-x} materials are anisotropic layered materials with sheets of metal chalcogenide.[15] The structure of the lanthanide dichalcogenides is derived from the ZrSSi aristotype and contains distorted rock salt double layers of $[Ln^{3+}X^{2-}]^+$ that alternate with sheets of chalcogenide $[X_n]^-$.[16] The exception is europium, $EuSe_2$, where the metal is divalent and the structure is more isotropic.[17] One difference between the two classes is that the TMDs have neutral layers and van der Waals interactions between the sheets, while the lanthanide dichalcogenides have a charged interlayer interaction that is more similar to ionic layered materials such as the "layered double hydroxides".[18] In addition to the formation of structural analogues of the TMD materials,[19] the properties are quite similar. For example, the LnX_{2-x} electronic properties range from semimetals to semiconductors[20] and exhibit charge density waves,[21,22] antiferromagnetism,[23] and superconductivity.[24] Unfortunately, the solid-state synthesis of these materials is challenging and requires increasingly high pressures across the series[25,26] due to the decomposition of LnX_{2-x} to form $X_2(g)$ and Ln_2X_3,[27] although polychalcogenide fluxes may provide a general route.[28]

Received: July 31, 2019
Revised: August 9, 2019
Published: August 12, 2019

DOI: 10.1021/acs.chemmater.9b03067
Chem. Mater. 2019, 31, 7779−7789

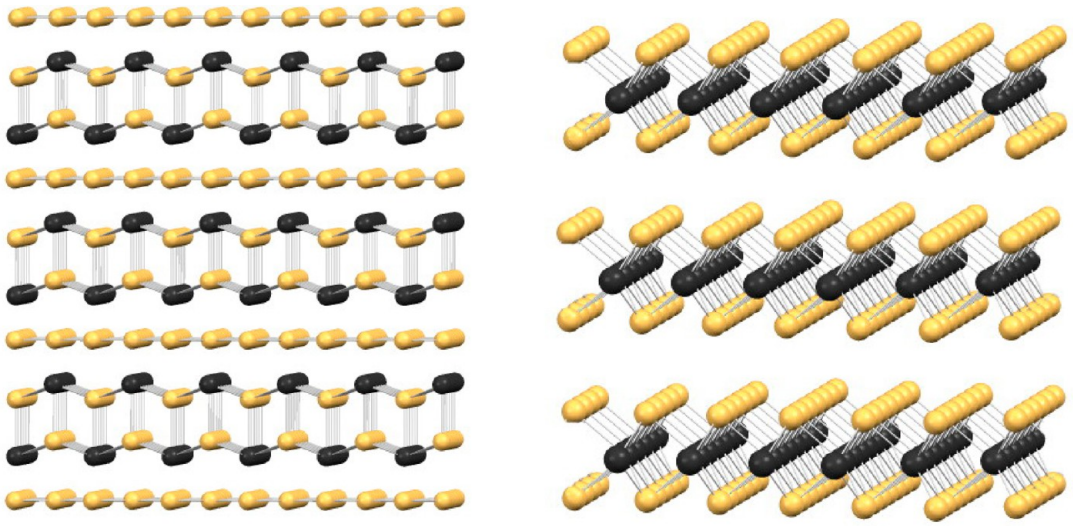

Figure 1. Comparison of the lanthanide dichalcogenide structure (left) with the transition metal dichalcogenide structure (right). The black atoms are metals, and the yellow atoms are chalcogens in both structures.

The synthesis of rare-earth chalcogenides is also challenging at the nanoscale. Despite the advantages of incorporating lanthanides into nanocrystalline metal chalcogenide hosts with intermediate band gaps,[29] the synthesis is hindered by the chemistry of the hard trivalent lanthanides, which have little affinity for the soft chalcogenides. There are many chalcogenide precursors that have been developed for elegant control of II−VI nanoparticle synthesis, such as the thio- and seleno-ureas.[30,31] These may be paired with a wide range of metal salts for the transition and main group metals used in nanoparticle synthesis, but the corresponding lanthanide salts are insoluble in nanoparticle solvents (e.g., halide salts) or use carboxylate ligands that inevitably lead to oxides or oxychalcogenide products. For example, the solution synthesis of $LnSe_2$ for (Ln = La−Nd and Eu) was reported using $Ln(acac)_3$ (acac = acetylacetonate) and SeO_2; however, this approach led to mixed-phase materials with $Ln_4O_4Se_3$. The smaller lanthanides (Ln = Sm−Ho) with this synthesis formed only $Ln_4O_4Se_3$.[32] Alternatively, nanoparticles of NdS_2 have been reported from the conversion of Nd_2O_3 nanoparticles using boron sulfides[33] but are unfortunately not solution processable. Brennan has synthesized a large number of novel lanthanide chalcogenide molecules and clusters, but they have not been adopted as precursors for nanoparticle synthesis because they are air-sensitive and synthetically demanding.[34−36] Single-source precursors for EuS have been dominated by the dithiocarbamates,[37−40] but recently, the precursor $Eu(X_2PPh_2)_3(THF)_2$ for X = S and Se (THF = tetrahydrofuran) was reported to form EuS and EuSe nanomaterials.[41] While the dithiocarbamate chemistry has been extended to other lanthanides,[42] we were interested in determining the range of materials formed from the diphenyl-diselenophosphinate complexes and discovered a general route to $LnSe_{2-x}$ nanosheets.

Here, we report the synthesis and single-crystal structures of $[Ln(Se_2PPh_2)_3(CH_3CN)_2]$for Ln = La−Ho (excluding Pm) and $Ln(Se_2PPh_2)_3(CH_3CN)$ for Ln = Er−Lu. Heating these precursors in solution under an inert environment led to phase pure nanosheets of the corresponding $LnSe_{2-x}$ for Ln = La−Ho, with two exceptions. The first was $CeSe_{2-x}$ that, on the basis of powder X-ray diffraction, also contained impurities of cerium oxide and cerium ultraphosphate. Second, although phase pure, the europium complex formed EuSe as reported previously.[41] Transmission electron microscopy (TEM) studies provided insight into the mechanism of nanosheet growth and, combined with atomic force microscopy (AFM), show that the thinnest materials were ∼4 nm. Raman spectroscopy was used to evaluate layer breathing modes,[43] as both peak position and intensity can vary due to interlayer interactions.[44] To demonstrate the synthetic feasibility, we also prepared the alloy, $Sm_{1-x}Gd_xSe_{1.8}$, which also formed nanosheets with a uniform composition.

EXPERIMENTAL SECTION

Materials. Oleylamine (>70%, Sigma), lanthanide(III) triflate [$Ln(OTF)_3$, where Ln = La, Ce, Sm, Eu, Dy, or Yb; 98%, Alfa Aesar], lanthanide(III) triflate [$Ln(OTF)_3$, where Ln = Pr, Nd Gd, Tb, Ho, Er, or Lu; 98%, Sigma], diethylamine (>99%, Sigma), diphenylphosphine (98%, Sigma), acetonitrile (>99%), absolute ethanol (>99.7%), and hexanes (>99.5%) were used as received. Quartz tubes were purchased from ChemGlass.

Synthesis of the Ligand and Complexes. *$[Et_2NH_2][Se_2PPh_2]$ (DSP salt) (1).* In an air-free atmosphere, selenium (7.894 g, 0.10 mol) was mixed with anhydrous ethanol (40 mL, 0.66 mol). Diphenylphosphine (8.7 mL, 0.05 mol) was added to the slurry. Excess diethylamine (5.3 mL, 0.051 mol) was injected into the reaction mixture, and it was lowered into a water bath at 60 °C and stirred for 60 min. The solution turned from black to a rust-red color over the course of the reaction. The reaction mixture was cooled to room temperature and then placed in a −30 °C freezer. A white precipitate formed and was vacuum filtered and washed with ethanol and diethyl ether to isolate the product in 58% yield. FTIR (cm^{-1}): 2990 (w), 2769 (w), 1539 (w), 1435 (w), 1088 (w), 750 (m), 694 (m), 537 (m), 512 (m), 470 (w), 449 (w). Anal. Cald. for $C[Et_2NH_2]$-$[Se_2PPh_2]$: C, 46.05; H, 5.33; N, 3.36. Found: C, 46.09; H, 5.30; N, 3.35.

$Ln(Se_2PPh_2)_3(MeCN)_x$. In an air-free atmosphere, $[Et_2NH]$-$[Se_2PPh_2]$ (**1**) (1.252 g, 3.0 mmol) was dissolved in acetonitrile (25 mL, 0.48 mol). $Ln(OTF)_3$ (1.0 mmol) was added directly to the ligand solution. The solution started to form a precipitate upon addition of the triflate salt and was stirred for 30 min. The product was isolated via gravity filtration and washed with acetonitrile. Details, including yields, FTIR data, elemental analysis, and observations, are provided in Supporting Information (sections S1 and S2) for Ln = La (**2**), Ce (**3**), Pr (**4**), Nd (**5**), Sm (**6**), Eu (**7**), Gd (**8**), Tb (**9**), Dy

DOI: 10.1021/acs.chemmater.9b03067
Chem. Mater. 2019, 31, 7779−7789

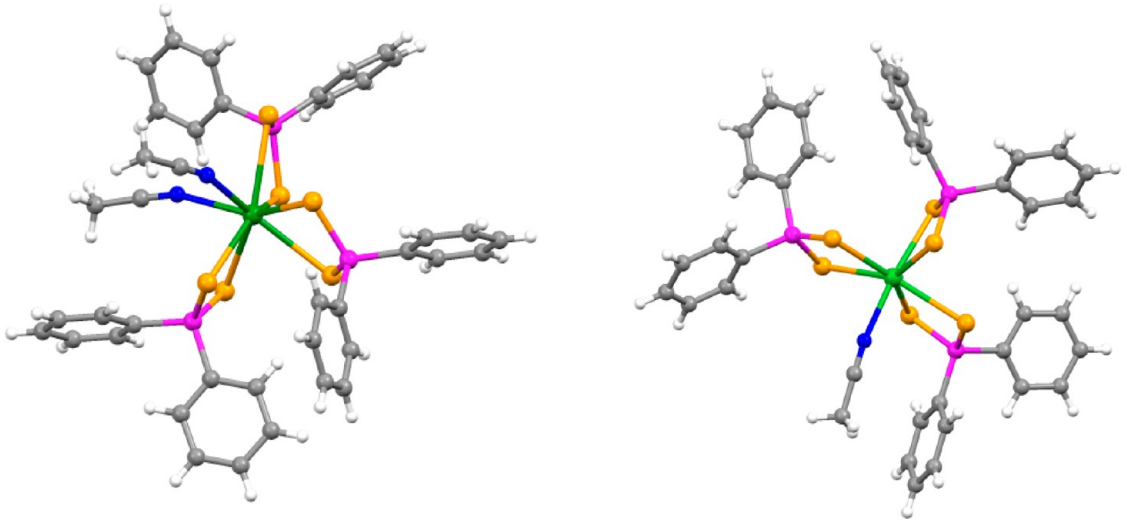

Figure 2. Representative structures of $Ln(Se_2PPh_2)_3(CH_3CN)_2$ (left) for Ln = La−Ho, but not Pm, and $Ln(Se_2PPh_2)_3(CH_3CN)$ (right) for Ln = Er−Lu.

(**10**), Ho (**11**), Er (**12**), Tm (**13**), Yb (**14**), and Lu (**15**). Note that synthesis and structures for $[Ln(Se_2PPh_2)_3(THF)_2]$ for Ln = La, Ce, and Nd were reported previously (THF = tetrahydrofuran),[45] and $[Ln(S_2PPh_2)_3(CH_3CN)_2]$ for Ln = Gd and Dy.[46]

Solventless Thermolysis. The complexes (∼0.20 g) were loaded into 8 in. quartz tubes. The tubes were evacuated and then sealed. The sealed tubes were heated in a furnace to 650 °C at a rate of 5 °C/min, kept at that temperature for 1 h, and cooled to 25 °C at a rate of 0.5 °C/min. The thermolysis product was collected and stored in a nitrogen glovebox.

Nanoparticle Synthesis. Oleylamine (10 mL) was degassed under vacuum at 110 °C for 1 h. The solution was switched from under vacuum to nitrogen, and the temperature of the reaction mixture was increased to 315−330 °C. The complex $Ln(Se_2PPh_2)_3(CH_3CN)_x$ (x = 1 or 2) (0.2 mmol) was dissolved in oleylamine (5 mL) under an inert atmosphere and injected into the hot oleylamine solution. A dark-colored precipitate (red for EuSe) formed within 1 min. The reaction occurred for 1 h at 330 °C, and then the mixture was cooled to room temperature. The precipitate was washed in hexanes and ethanol in four cycles and stored in hexanes.

Characterization. Elemental analysis (C, H, N) was performed on a PerkinElmer 2400 microanalyzer using acetanilide as a standard. FTIR measurements were recorded in the range of 400−4000 cm^{-1}, from pressed pellets in KBr on a PerkinElmer FTIR instrument. Thermal analysis was performed on a model Q50 TA Instruments thermogravimetric analysis (TGA) instrument. Simultaneous TGA-DTA data were measured on samples in a platinum pan from 25 to 800 °C under a N_2 flow of 10 mL/min. The heating rate was 5 °C/min. X-ray powder diffraction patterns were obtained using a Rigaku Ultima IV X-ray powder diffractometer with Cu Kα radiation at 40 kV and 30 mA and a D/teX silicon strip detector. Samples were prepared for TEM measurements by drop casting dilute nanomaterial solutions on carbon-coated copper TEM grids. High-resolution TEM (HRTEM) and energy dispersive X-ray spectroscopy (EDS) analyses were performed on a JEOL JEM-2100F FEG TEM instrument operated at 200 kV at the Advanced Imaging and Microscopy Lab at the University of Maryland. Scanning electron microscopy (SEM) images were taken with a Zeiss SUPRA 55-VP scanning electron microscope, at an acceleration voltage of 20 kV with an in-lens detector. Raman spectroscopy was performed with a Horiba Raman microscope equipped with a 532 nm laser and a 1800 line/mm grating and calibrated against a diamond standard. The instrument was interfaced with an Olympus BH2-UMA optical microscope, and a magnification factor of 100× was typically used. Spectra were recorded in extended scan mode from 100 to 3200 cm^{-1} and analyzed using the WiRE 2.0 software package. The surface topography was acquired with an NTEGRA scanning probe microscope (NT-MDT) operated in semicontact/tapping mode. The probe is made from single-crystal silicon with a nominal cantilever spring constant of ∼12 N/m.

X-ray Crystallography. Intensity data were collected on a Bruker D8 Quest CMOS diffractometer using Mo Kα radiation (λ = 0.71073 Å). The data were integrated using the SAINT suite of software, and absorption corrections were calculated using SADABS. Crystal structures were determined and refined using the SHELX-2013 and -2016 packages, with the assistance of X-Seed. The structures were determined using direct methods and refined by full-matrix least-squares methods with anisotropic thermal parameters for all non-hydrogen atoms. Hydrogen atoms were located in calculated positions and refined isotropically. Crystallographic details and additional refinement information are provided in section S2 of the Supporting Information. A summary of structural details is provided in Table S3.

RESULTS AND DISCUSSION

Synthesis and Structures of $[Ln(Se_2P(Ph)_2)_3(CH_3CN)_x]$ (x = 1 or 2). The bidentate diselenophosphinate ligand, $[Se_2PR_2]^-$, can be prepared from a variety of secondary phosphines, as described by Artem'ev,[47] and in principle, the R group can be tailored to tune solubility. The complexes formed almost immediately upon addition of the ligand, and crystals grew easily. Although air-sensitive, they can be prepared under inert conditions and stored in a glovebox. In contrast to the dithiocarbamate ligand, which forms complexes of the type $Ln(S_2CNEt_2)_3L$ (L = phenanthroline or bipyridine), the diselenophosphinate can fill the coordination sphere with solvent to yield complexes of the type $Ln(Se_2PPh_2)_3(CH_3CN)_2$, shown in Figure 2. The coordination number of 8 is the same for complexes of both ligands and higher than for transition metals, as expected for the larger lanthanides. It appears the dithiocarbamate can bridge two metals more easily, leading to catenation and an amorphous precipitate that does not occur with the diselenophosphinate. The dithiocarbamate complexes require a planar bidentate ligand, whereas the diselenophosphinate complexes complete the coordination number with the solvent. The individual structures of the lanthanide diselenophosphinates were unsurprisingly similar. The single-crystal structure of the first in the series $La(Se_2PPh_2)_3(CH_3CN)_2$ and the THF versions

DOI: 10.1021/acs.chemmater.9b03067
Chem. Mater. 2019, 31, 7779−7789

$Ln(Se_2PPh_2)_3(THF)_2$ for La, Ce, and Nd have been reported,[48] as have the structures of $[Ln(S_2PPh_2)_3(CH_3CN)_2]$ for Ln = Gd and Dy.[46]

The reason for determining the structures for the entire series was to observe periodic trends for complexes with the same ligand (diphenyl-diselenophosphinate) and the same solvent (acetonitrile). The series provided insight into phase formation because the coordination number of the precursors exhibits a break that has not been reported for these complexes between Ln = La–Ho forming $[Ln(Se_2PPh_2)_3(CH_3CN)_2]$ (8-coordinate) and Ln = Er–Lu forming $[Ln(Se_2PPh_2)_3(CH_3CN)]$ (7-coordinate). The lanthanide contraction causes a systematic change in ionic radii, but the change in coordination number leads to an offset in the average Ln–Se bond lengths for Ln = Er–Lu, as shown in Figure 3. In a study of the high-temperature solid-state

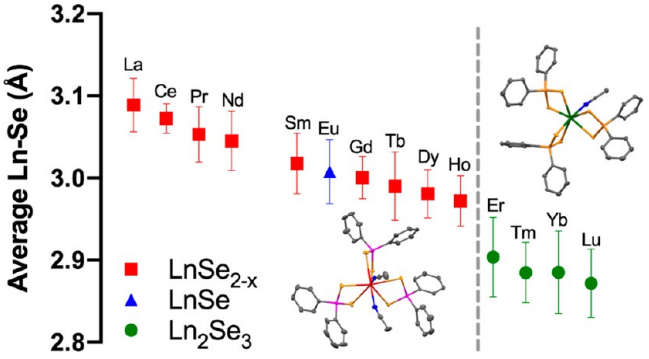

Figure 3. Average Ln–Se bond length vs Ln for the $Ln(Se_2PPh_2)_3(CH_3CN)_x$ structures that have been determined. The vertical bar indicates the range of Ln–Se bond lengths observed in each complex. The color and shape indicate the phase formed under nanoparticle conditions; the lanthanides with red squares form $LnSe_2$, the blue triangle LnSe, and green circles Ln_2Se_3.

synthesis of $LnSe_2$ materials, Doert was unable to prepare the $LnSe_{2-x}$ beyond Ho (at 8 GPa), presumably because the thermodynamic stability for the sesquiselenide is greater than that for the diselenide for Er–Lu.[49] We also observe a break between Ho and Er in our nanoparticle synthesis (*vide infra*) leading to the stabilization of a different phase for the smaller lanthanides, demonstrating the value of structural comparisons across molecules, solid-state bulk, and nanomaterials.

Thermolysis Studies. To evaluate the thermal stability of the precursors, we used TGA and found that all of the precursors lose acetonitrile at ~100 °C, followed by a second thermal decomposition between 200 and 400 °C. Air-stable precursors of the dithiocarbamate, $[Ln(S_2CNEt_2)_3Phen]$ (Phen = phenanthroline), thermally decompose with an onset temperature that decreased as the lanthanide ionic radius decreased.[42] However, the trend for the $[Ln(Se_2PPh_2)_3(CH_3CN)_x]$ complexes was complicated by oxidation of the precursors during our TGA measurements, confounding the product formed by weight loss as well as the temperature of decomposition.

We frequently use solventless solid-state thermolysis of precursors to determine the thermodynamic product formed at high temperatures to compare with solution reactions under nanoparticle synthetic conditions. Both the solventless thermolysis and the nanoparticle syntheses gave the same product in all cases but for europium. When $[Eu(Se_2PPh_2)_3(CH_3CN)_2]$ was thermally decomposed, the product identified by X-ray powder diffraction was $Eu_2P_2Se_6$ (see S5 of the Supporting Information),[50] whereas under nanoparticle solution conditions, the product was EuSe (S6 of the Supporting Information). Similarly, O'Brien has shown that conditions like temperature and ligand structure for nanoparticle or chemical vapor deposition affect whether a metal phosphide or selenide phase is stabilized for nickel and cobalt diselenophosphinate precursors.[51−53] Europium is distinct for the preference of the divalent state when bonded to soft donors, as found for EuSe and $Eu_2P_2Se_6$, but the final phase formed may reflect a different mechanism of bond dissociation in the solid state versus in solution. What is interesting is that europium in $EuSe_2$ is also divalent yet not observed under these conditions. It is worth noting that cerium diselenide exhibited two impurity phases (see S4 of the Supporting Information), one containing a mixed valent oxide $(Ce^{3+})_4(Ce^{4+})_3O_{12}$[54] and the second an oxidized phosphorus, $Ce(P_5O_{14})$, emphasizing the role both valence and ligand stability play in product formation.

For the four smallest lanthanides, Ln = Er–Lu, the solventless thermolysis produced what appears to be the Ln_2Se_3 structure. There is an ambiguity for the redox active lanthanides, which can form divalent rock salt LnSe or trivalent Ln_2Se_3. Because Tm_2Se_3 and Yb_2Se_3 exhibit the Sc_2S_3 structure, a superstructure with ordered cation voids of the NaCl structure,[55] it is very difficult to distinguish from the monochalcogenide on the basis of powder diffraction (see S10 of the Supporting Information). We attempted to use EDS to determine the composition, but the Ln:Se ratios were not clear-cut. The oxidation state is another way of distinguishing the two materials, $Ln^{III}{}_2Se_3$ and $Ln^{II}Se$. The stability of the divalent state is generally thought to decrease in the following order: $Eu^{2+} > Yb^{2+} > Sm^{2+} > Tm^{2+}$.[55] This brackets the reducing ability of the ligand by the products formed. The ligand is strong enough to reduce Eu(III) in the complex to Eu(II) in EuSe (the easiest metal to reduce); however, in the case of samarium, the trivalent complex forms $Sm^{III}Se_{2-x}$, indicating the ligand is not strong enough to reduce Sm(III). Of the four redox active lanthanides, Tm is the most challenging to reduce, so it seems unlikely that Tm would be reduced to form TmSe if Sm is not reduced by the diselenophosphinate. Therefore, the phase is assumed to be Tm_2Se_3, following reasoning similar to that used to explain the formation of Tm_2Se_3 from thermolysis of $Tm(SePh)_3$.[56] The reduction potential for Yb lies between those of Eu and Sm, so the question of whether our products are YbSe or Yb_2Se_3 remains without X-ray absorption studies or another technique used to determine the oxidation state.

Nanosheet Synthesis. The synthesis of TMD nanosheets is achieved through the careful control of the nucleation rate, either by slow injection or by the use of slowly decomposing precursors, as well as solvents that selectively favor lateral growth.[57] $LnSe_{2-x}$ nanosheets were observed for a wide range of lanthanides (Ln = La–Ho) as shown in Figure 4 and were all synthesized under the same conditions via hot injection of $Ln(Se_2PPh_2)_3(CH_3CN)_x$ (x = 1 or 2) in oleylamine (330 °C, 1 h). Under these conditions, the reaction is quite rapid. The solution color changes from orange to dark red after injection followed by a dark brown-black precipitate. For the smallest lanthanides, Er–Lu, higher concentrations of the complex were required for product formation and the material formed was too poorly crystalline for phase determination. The mechanism of conversion kinetics of this ligand can be altered by the

DOI: 10.1021/acs.chemmater.9b03067
Chem. Mater. 2019, 31, 7779−7789

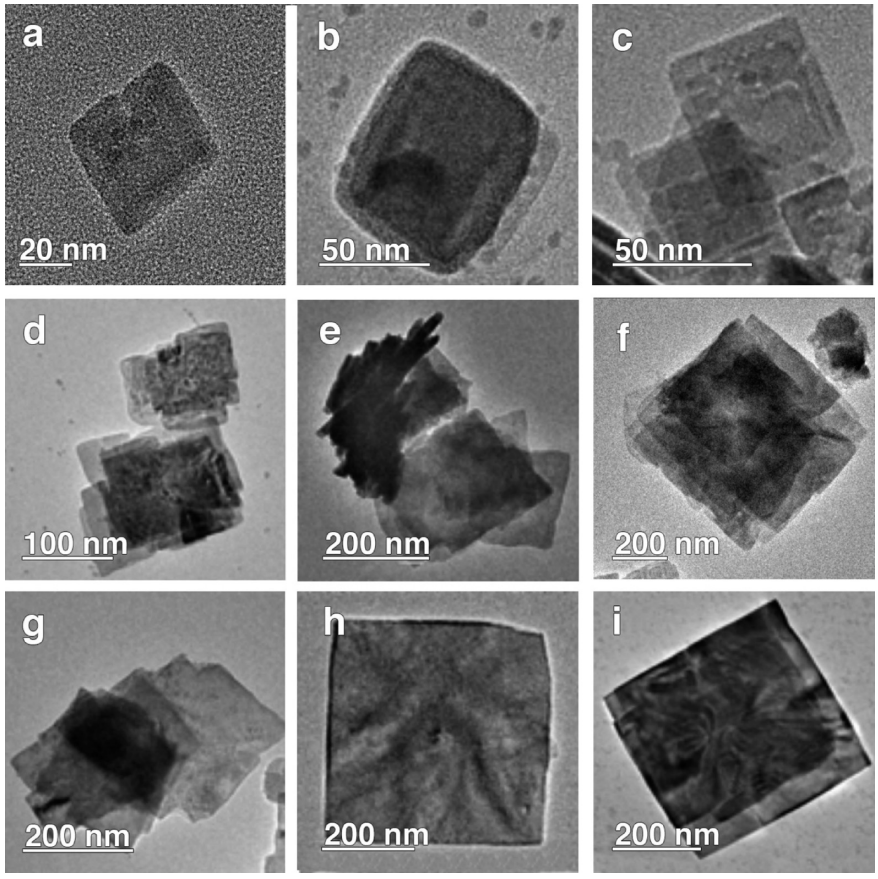

Figure 4. TEM of the $LnSe_{2-x}$ nanosheets for (a) $LaSe_{2-x}$, (b) $CeSe_{2-x}$, (c) $PrSe_{2-x}$, (d) $NdSe_{2-x}$, (e) $SmSe_{2-x}$, (f) $GdSe_{2-x}$, (g) $TbSe_{2-x}$, (h) $DySe_{2-x}$, and (i) $HoSe_{2-x}$.

addition of a carboxylate, as Owen has demonstrated using $[Cd(S_2PPh_2)_2]$;[58] however, this approach would inevitably lead to oxidation here.

Phase Stability. Phase control is a fundamental question that has gained importance as the synthesis of nanomaterials has extended beyond II−VI semiconductor materials. The formation of $LnSe_{2-x}$ rather than Ln_2Se_3 was somewhat surprising because we have previously reported that the thermolysis of $[Ln(S_2CNEt_2)_3Phen]$ complexes forms polytypes of Ln_2S_3 for all lanthanides. Unfortunately, the sulfur version of $Ln(S_2PPh_2)_3(solvent)_x$ complexes (under solventless thermolysis in sealed tubes) led to amorphous products preventing a direct comparison with the dithiocarbamate. Phase control has been linked to the reactivity of the precursor in kinetically controlled systems. For example, different chain length dialkyl disulfides and thiols can be used with $FeCl_2$ to control product formation to give FeS_2, Fe_3S_4, or Fe_7S_8.[59] Analogously, different dialkyl diselenide precursors were used to control the composition of a $Cu_{2-x}Se$ intermediate that dictated whether $CuInSe_2$ chalcopyrite versus wurtzite (the metastable phase) is favored.[60] Although the stoichiometry of the complexes has chalcogen in excess for both the dithiocarbamate and diselenophosphinate precursors (1:6 Ln:X), the higher Se concentration in $LnSe_{2-x}$ may be favored as a result of the increased reactivity of selenium compared with sulfur.[78]

The nonstoichiometry of $LnSe_{2-x}$ in the solid state also paralleled that of the nanosheets in the periodic trend for the value of x. Nonstoichiometry has been explained as a result of the mismatch of the rigid frame $[Ln^{3+}Se^{2-}]$, which cannot accommodate the square lattice of Se for the smaller lanthanides. As a result, the larger lanthanides can support a stoichiometric Ln:Se ratio of 1:2 under pressure but otherwise exhibit Se vacancies forming $LnSe_{1.9}$ for Ln = La−Nd and $LnSe_{1.8}$ for Ln = Sm−Ho. An electronic consideration of the selenium layer leads to a similar conclusion in which the excess electrons can be delocalized in polyanions; otherwise, vacancies form.[16] Stoichiometric $LnSe_2$ has a square sheet of selenium (tetragonal symmetry), but nonstoichiometry reduces the symmetry and forms square nets of a herringbone pattern of Se_2^{2-} dimers (for $LnSe_{1.9}$)[61] or vacancies that lead to single Se^{2-} anions as found in $LnSe_{1.8}$.[62] With small metals, like the diselenide $DySe_{1.84}$, an incommensurate superstructure due to Se defects can be observed in the electron diffraction pattern.[21] We see this reflected in the powder diffraction patterns that match the change in stoichiometry across the lanthanide series prepared in the solid state. S8 and S9 of the Supporting Information provide a comparison of the $LnSe_{1.9}$ versus $LnSe_{1.8}$ powder diffraction patterns.

Nanosheet Thickness. One of the reasons there have been few reports of solution-phase synthesis of TMDs is that controlling the growth to form single-layer 2D sheets is challenging.[63] There are examples of solution-grown nanosheets with thickness tuning. For example, Schaak reported a series of SnSe nanosheets with thicknesses from 35 to 8 nm tuned through precursor control.[64] Although we have not systematically investigated thickness tuning here, the whole range of lanthanide diselenide materials exhibit highly

DOI: 10.1021/acs.chemmater.9b03067
Chem. Mater. 2019, 31, 7779−7789

anisotropic growth. The X-ray powder diffraction pattern of drop-cast nanosheets exhibited a significant preferred orientation (see Figure 5), confirming that the bulk material exhibits the same nanosheet morphology observed by SEM and TEM. The high-intensity (00*l*) peaks and diminished (*hk*0) peaks are consistent with HRTEM analysis, which suggests that the nanosheet face is normal to the [00l] direction and that isolated nanosheets are single crystal from the face and side views as shown in Figure 6.

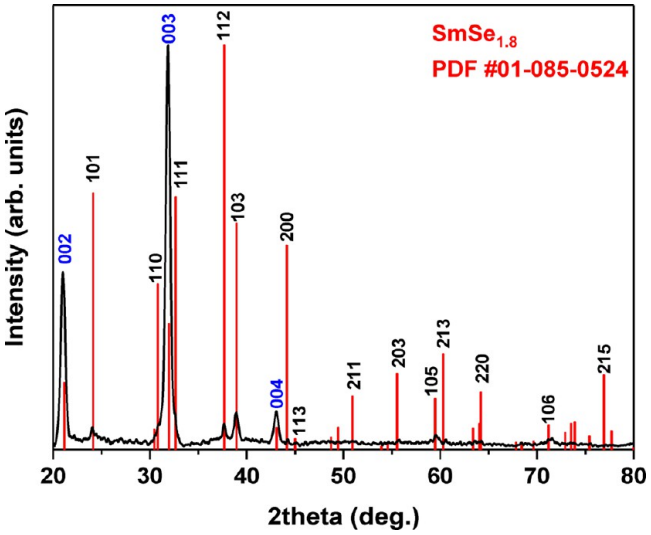

Figure 5. X-ray powder diffraction pattern for of drop cast films of $SmSe_{2-x}$. The 00*l* peaks are enhanced (blue) and the *hk*0 peaks are diminished due to the preferred orientation of the nanosheets.

We have used both TEM and AFM to evaluate the nanosheet thicknesses and focused on $SmSe_{2-x}$ as being representative of the series. The side-view TEM image of a single crystalline nanosheet has ~8 Å per layer, as expected for a *c*-axis value for $SmSe_{1.9}$ of 8.0 Å (Figures 6b and 7d). This is consistent with the preferred orientation analysis of the powder X-ray data. Both SEM and TEM of $SmSe_{2-x}$ provided examples of isolated and aggregated nanosheets based on face and side views, as shown in Figure 7 for $SmSe_{2-x}$. By imaging a collection of stacked nanosheets (Figure 7), we were able to obtain histograms of the nanosheet dimensions. Only nanosheets with clear edges were used to define the thickness (such as in Figure 7c), and the lengths were consistent with the TEM image of the face of the nanosheet. After 1 h, the average thickness was 11 ± 2 nm and the lateral length was 190 ± 50 nm (the histogram from 150 crystals is shown in Figure 8). Several studies using AFM determined the nanosheets to be ~4 nm thick, as shown in Figure 9 (and S12 of the Supporting Information), which corresponds to approximately five unit cells.

Raman Spectroscopy. The lattice vibrations of few-layer thick materials begin to shift in position and intensity due to

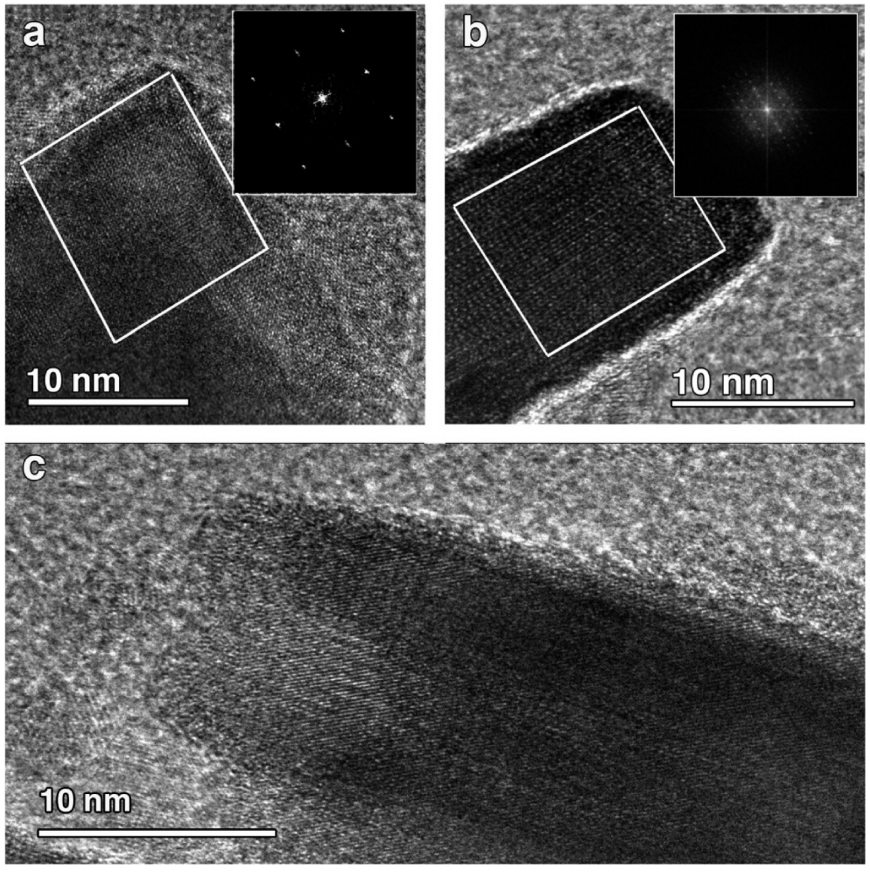

Figure 6. (a) High-resolution TEM image of the $SmSe_{1.8}$ nanosheet face with Fourier transform demonstrating the cubic symmetry with the cube edge measured to be 4.8 Å (*a* = 4.1 Å). (b) HRTEM image of the edge or side view of the $SmSe_{1.8}$ nanosheet and Fourier transform (layer separation close to *c* = 8.0 Å).[83] (c) HRTEM image of two side-view $SmSe_{1.8}$ nanosheets coalescing.

DOI: 10.1021/acs.chemmater.9b03067
Chem. Mater. 2019, 31, 7779−7789

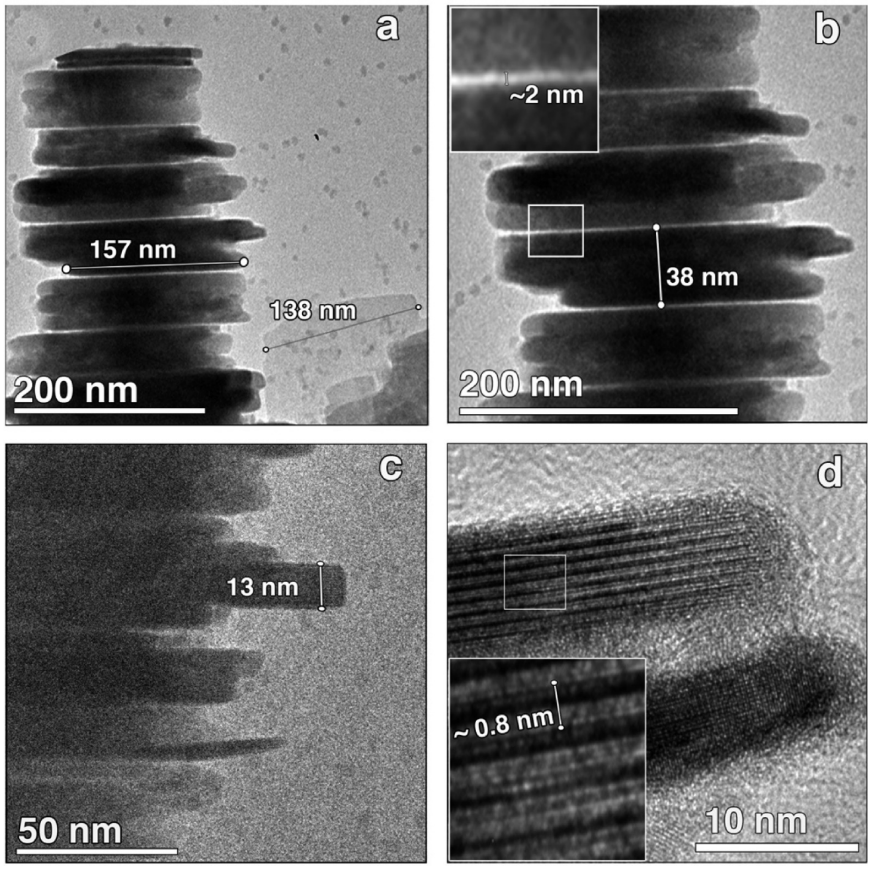

Figure 7. TEM study of $SmSe_{1.8}$ nanosheets grown at 330 °C. (a) Dimensions of the lateral face of the nanosheet, where ~140 nm is the average of the stacked nanosheets (a select sheet is 157 nm). (b) Nanosheets aggregate into 38 nm plates. Stacked plates are separated by a fine bright line of ~2 nm that corresponds to the length of the oleylamine. (c) Blocks of nanosheets have stepped edges, which average 4−15 nm thick nanosheets. (d) Side edge of an ~6.7 nm thick single-crystal nanosheet with ~0.8 nm layers, which is close to the *c*-axis of 8.0 Å.

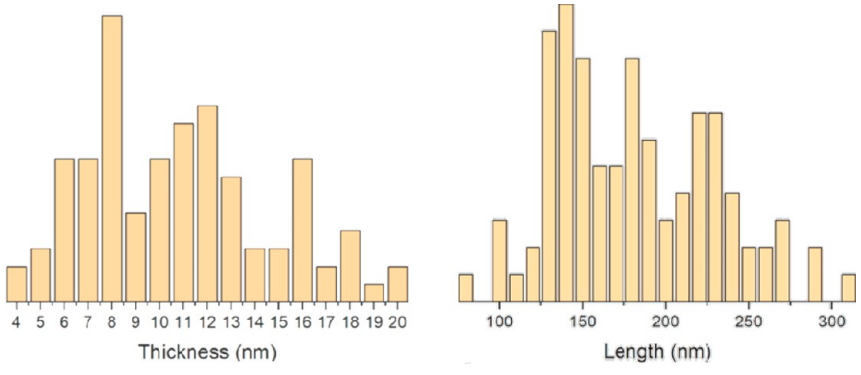

Figure 8. Histogram of $SmSe_{1.8}$ nanosheet length and thickness (of 150 sheets).

the loss of translational symmetry in the *z*-axis. The only Raman spectrum reported for the $LnSe_{2-x}$ materials is that of $LaSe_{2-x}$, in addition to another report of $LaSe_{2-x}S_x$ alloys, so a general comparison between the solid state and nanosheets was not possible.[65,66] The Raman spectroscopy was sharpest for the $LaSe_{2-x}$ nanosheets reported here (see S14 of the Supporting Information) and matched the reported solid-state product. The low-energy peak, at ~80 cm^{-1}, while broad for lanthanides smaller than La, does appear to systematically shift to a lower energy as might be expected for the heavier metals. By washing with trioctyl phosphine, we could remove any Se occasionally observed in the diffraction pattern. Raman is quite sensitive in identifying Se[67] and has peaks that overlap with the three $CeSe_{2-x}$, $NdSe_{2-x}$, and $HoSe_{2-x}$ nanosheets.

Growth Mechanisms. There are three common mechanisms for 2D nanomaterials grown from solution: growth driven by screw dislocations, oriented attachment, and surfactant-guided growth.[68] The lanthanide diselenides have different types of bonding within and between layers, so it is not surprising they naturally grow anisotropically. There is evidence of the first two growth mechanisms here. The evidence for screw-dislocation growth is most clearly seen in nanosheets prepared below ~315 °C, as one can see in the left SEM image in Figure 10 (more examples are given in S13 of the Supporting Information). Screw-dislocation growth most

DOI: 10.1021/acs.chemmater.9b03067
Chem. Mater. 2019, 31, 7779−7789

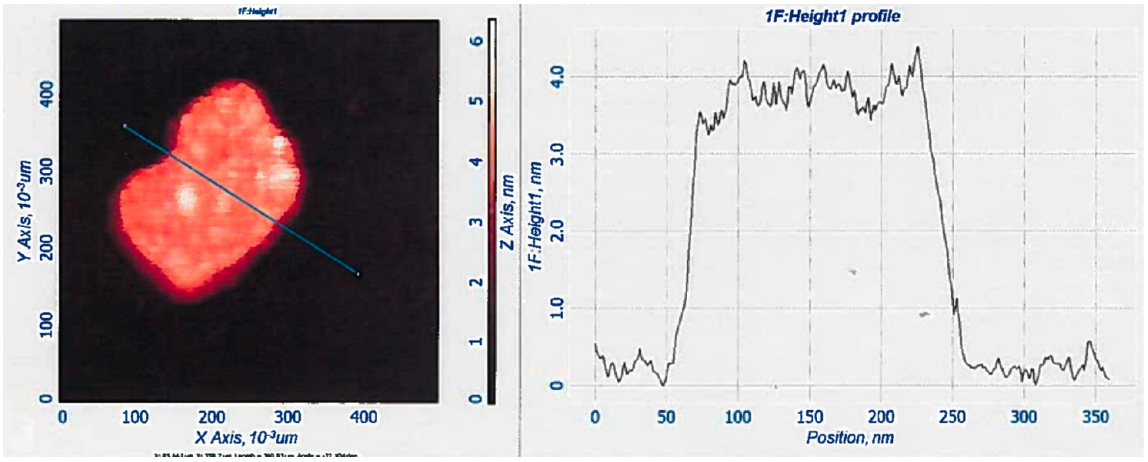

Figure 9. Atomic force microscopy data of $SmSe_{1.8}$ (left) and corresponding height profile (right).

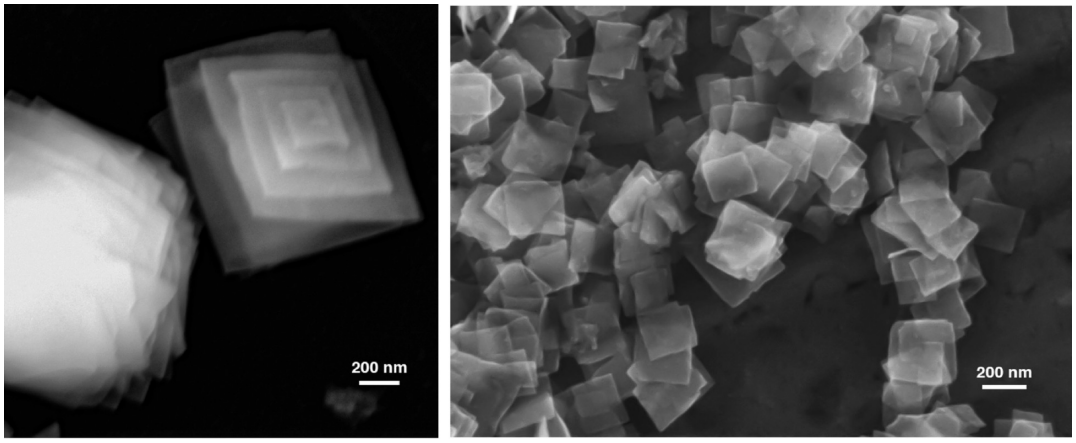

Figure 10. SEM images of $SmSe_{2-x}$, exhibiting spiral nanosheet growth from solution at 315 °C (left) and flat stacked sheets from solution at 330 °C (right).

commonly occurs under low supersaturation conditions, which may be due to the lower temperatures used.[69] By contrast, the nanosheets grown at 330 °C lack evidence of spiral growth, as one can see in Figure 10 (right).

For reactions at higher temperatures, the lateral dimensions of the nanosheet square face range between 100 and 300 nm, for $SmSe_{2-x}$, and exhibit evidence of nanosheet stacking. In Figure 6a, the HRTEM image of the edge of a square with the Fourier transform suggests the nanosheets are single-crystalline and confirms the tetragonal symmetry of the face. We also observe many examples of side views of 4−16 nm thick nanosheets as shown in Figure 7. The self-assembly of the nanosheets with a common crystallographic orientation is consistent with an oriented attachment.[70] The TEM studies also show aggregation and joining at the planar interface as shown in Figure 6c, which shows two nanosheets that have coalesced during growth. One of the distinctions between Oswald ripening and oriented attachment is a bimodal distribution in the size histogram.[71] The histogram of nanosheet thicknesses (Figure 8) exhibits a multimodal character with the highest distributions for multiples of the smallest 4 nm nanosheet (8, 12, and 16 nm), consistent with oriented attachment growth. The two growth mechanisms are not incompatible; spiral growth may occur during oriented attachment when there is a small misorientation at the interface.[72]

In addition to the evidence that the nanosheets aggregate through oriented attachment, the aggregates form ∼40 nm plates. In Figure 7a−c, aggregates of nanosheets can be seen where the edges are stepped due to the differing dimensions of the individual nanosheets. Interestingly, the plates are also stacked, where the separation of plates is defined by a ∼2 nm thick bright flat line (inset of Figure 7b). The thickness of the bright line is very close to that expected for a monolayer of oleylamine. The range of lateral dimensions suggests the nanosheets form first and then aggregate in solution, with the *c*-axis aligned as expected from oriented attachment. However, the plates form coherent stacks in which the *c*-axis is again aligned, with a highly ordered and densely packed oleylamine layer in the space between them. This suggests that the ligand must play a role in the hierarchical assembly of plates. The stacked plates are reminiscent of mesocrystals, but this is usually thought to be an intermediate step in oriented attachment.[73] The mechanism driving nanosheet aggregation is likely the ionic nature of the layers, but it is unclear why the lamellar assembly of stacked "plates" separated by a capping ligand forms so distinctly.

In-Plane Alloys of $Sm_{1-x}Gd_xSe_{1.8}$. To demonstrate the synthetic versatility of the precursors and further probe the nanosheet growth mechanism, we have investigated Sm and Gd metal alloy formation. For TMDs, alloys are stabilized by having close lattice constants and similar metal−chalcogen

DOI: 10.1021/acs.chemmater.9b03067
Chem. Mater. 2019, 31, 7779−7789

bond lengths.[74] Alloys of in-plane TMD nanosheets have been formed for both anion (e.g., $MoS_{2-x}Se_x$) and cation alloys ($Mo_{1-x}W_xS_2$) to tune the band gap or conductivity.[75] In most cases, alloys were synthesized by CVD, or exfoliation from single crystals,[76] with few reports of solution synthesis of alloyed TMD nanosheets. In the case of $MoSe_{2-x}S_x$, the nanosheets from oleylamine, Se, and dodecanethiol, the S composition was quite low at ~2%.[77] This is consistent with studies of alloyed nanoparticles in which the reactivity of the chalcogenide has an influence over the final composition, and generally, Se is more reactive than S.[78] Using two precursors that form the same nonstoichiometric $LnSe_{1.8}$, the Sm and Gd complexes in a ratio of 4:1 were used to form $Sm_{1-x}Gd_xSe_{1.8}$, where $x \sim 0.2$. The rate of monomer formation for the Sm and Gd complexes must be reasonably similar; otherwise, the composition would reflect a higher concentration of the more reactive metal. Using GSAS, it was possible to refine both the cell constants and the Sm:Gd ratio (see S16 of the Supporting Information), for which the cell constant was slightly smaller as expected for the low composition of the smaller gadolinium, and the composition refined to $x = 0.2$ like the composition determined by EDS (78.7:21.3 Sm:Gd metal ratio). Finally, the line scans of EDS of the alloyed nanosheets appear to be uniform (see S15 of the Supporting Information), also indicating that composition is homogeneous across the nanocrystal.

Alloys are one route to tune properties, and we are also interested in determining whether the solution synthesis can be used to form single- and few-layer nanosheets. However, layered materials present a wide range of synthetic opportunities from intercalation to exfoliation and reassembly. There are examples of solution-grown nanosheets similar to those reported here that have been converted to single layers and a few layers through Li intercalation and sonication.[79] Recently, by taking advantage of the ability to intercalate copper between the layers in $LaSe_2$, Sasaki et al. were able to topotactically convert the lanthanide diselenide in the solid state to $LaCuSe_2$.[80] It should be possible to extend similar reactions to solution conditions. Alternatively, for reassembly of exfoliated nanosheets, it may be possible to reassemble lanthanide diselenide single layers with transition metal dichalcogenide single layers to form misfit materials as reported for $(LnS)_{1+x}TS_2$.[81] Under certain conditions, misfit layered compounds can also form novel nanotubes.[82]

CONCLUSIONS

We have identified new precursors for synthesizing thin $LnSe_{2-x}$ nanosheets for lanthanides from lanthanum to holmium. The precursors provide a route to a class of materials that are strongly similar to the TMDs and grow anisotropically in oleylamine. The molecular structure, solid-state products, and nanosheets formed from solution provide structural evidence of a break between Ho and Er in coordination number preference in the selenides. The products for the nanosheets are phase pure except for cerium. Generally, the redox active metals deviate: Ce by forming the mixed-valent Ce_7O_{12} and Eu by forming divalent EuSe. A question remains whether Yb forms YbSe or Yb_2Se_3, which we intend to investigate further. There is evidence of 2D growth by screw dislocations leading to spiral nanosheet growth at lower temperatures ($T < 315$ °C), while at higher temperatures, there is evidence of oriented attachment of nanosheets to form many-layer nanoplates. Alloy formation has been demonstrated for $Sm_{2-x}Gd_xSe_{1.8}$ nanosheets with a homogeneous composition across the layer. Future work will explore the potential for solution-grown single-sheet or few-layer materials and whether alloys, intercalation, exfoliation, or reassembly can tune the properties of these materials.

ASSOCIATED CONTENT

Supporting Information

The Supporting Information is available free of charge on the ACS Publications website at DOI: 10.1021/acs.chemmater.9b03067.

Synthetic details for the complexes (section S1), crystallographic details and additional refinement information (section S2), a summary of the structures (Table S3), powder diffraction data (S4–S10), TEM images (S11), AFM images (S12), SEM images (S13), Raman spectra (S14), TEM images with EDS line scans (S15), and GSAS refinement of $Sm_{0.8}Gd_{0.2}Se_{1.8}$ compared to the cell constant for $SmSe_{2-x}$ and $GdSe_{2-x}$ (S16) (PDF)

AUTHOR INFORMATION

Corresponding Author

*E-mail: sls55@georgetown.edu.

ORCID

Sarah L. Stoll: 0000-0001-7184-8672

Notes

The authors declare no competing financial interest.

X-ray crystallographic files in CIF format for compounds **3**–**15** were deposited in the Cambridge Structure Database with CCDC numbers 1918513, 1918512, 1918511, 1866356, 1866357, 1918517, 1918516, 1918518, 1918515, 1918514, 1866358, 1866359, and 1918510, respectively.

ACKNOWLEDGMENTS

The authors thank the National Science Foundation for supporting this work through Grants CHE-1607905 and CHE-1904616 and the Fulbright Foundation. O.S. thanks the Healy Foundation for support. The authors also thank Xinran Zhang for his assistance with AFM and the shared facility managed by the Institute for Soft Matter Synthesis and Metrology at Georgetown University.

REFERENCES

(1) Whittingham, M. S. Chemistry of Intercalation Compounds: Metal Guests in Chalcogenide Hosts. *Prog. Solid State Chem.* **1978**, *12*, 41–99.

(2) Rouxel, J., Ed. *Crystal Chemistry and Properties of Materials with Quasi-One-Dimensional Structures*; Reidel: Dordrecht, The Netherlands, 1986.

(3) Whittingham, M. S.; Jacobson, A. J. *Intercalation Chemistry*; Academic: New York, 1982.

(4) Butler, S. Z.; Hollen, S. M.; Cao, L.; Cui, Y.; Gupta, J. A.; Gutiérrez, H. R.; Heinz, T. F.; Hong, S. S.; Huang, J.; Ismach, A. F.; et al. Progress, Challenges, and Opportunities in Two-Dimensional Materials Beyond Graphene. *ACS Nano* **2013**, *7*, 2898–2926.

(5) Geim, A. K.; Novoselov, K. The Rise of Graphene. *Nat. Mater.* **2007**, *6*, 183–191.

(6) Lee, C.; Wei, X.; Kysar, J.; Hone, J. Measurement of the Elastic Properties and Intrinsic Strength of Monolayer Graphene. *Science* **2008**, *321*, 385–388.

(7) Novoselov, K. S.; Geim, A. K.; Morozov, S. V.; Jiang, D.; Katsnelson, M. I.; Grigorieva, I. V.; Dubonos, S. V.; Firsov, A. A. Two-

DOI: 10.1021/acs.chemmater.9b03067
Chem. Mater. 2019, 31, 7779–7789

Dimensional Gas of Massless Dirac Fermions in Graphene. *Nature* **2005**, *438*, 197−200.
(8) Mak, K. F.; Lee, C.; Hone, J.; Shan, J.; Heinz, T. F. Atomically Thin MoS_2: a New Direct-Gap Semiconductor. *Phys. Rev. Lett.* **2010**, *105*, 136805−4.
(9) Zhang, X.; Lai, Z.; Ma, Q.; Zhang, H. Novel Structured Transition Metal Dichalcogenide Nanosheets. *Chem. Soc. Rev.* **2018**, *47*, 3301−3338.
(10) Jariwala, D.; Sangwan, V. K.; Lauhon, L. J.; Marks, T. J.; Hersam, M. C. Emerging Device Applications for Semiconducting Two-Dimensional Transition Metal Dichalcogenides. *ACS Nano* **2014**, *8*, 1102−1120.
(11) Zhang, X.; Lai, Z.; Ma, Q.; Zhang, H. Novel Structured Transition Metal Dichalcogenide Nanosheets. *Chem. Soc. Rev.* **2018**, *47*, 3301−3338.
(12) Lv, R.; Robinson, J. A.; Schaak, R.; Sun, D.; Sun, Y.; Mallouk, T.; Terrones, M. Transition Metal Dichalcogenides and Beyond: Synthesis, Properties, and Applications of Single- and Few-Layer Nanosheets. *Acc. Chem. Res.* **2015**, *48*, 56−64.
(13) Xu, J.; Chen, X.; Xu, Y.; Du, Y.; Yan, C. Ultrathin 2D Rare-Earth Nanomaterials: Compositions, Syntheses, and Applications. *Adv. Mater.* **2019**, *306*, 1806461−17.
(14) Feng, W.; Sun, L.-D.; Zhang, Y.-W.; Yan, C. U.-H. Synthesis and Assembly of Rare Earth Nanostructures Directed by the Principle of Coordination Chemistry in Solution-Based Process. *Coord. Chem. Rev.* **2010**, *254*, 1038−1053.
(15) Wang, R.; Steinfink, H. The Crystal Chemistry of Selected AB_2 Rare Earth Compounds with Selenium, Tellurium, and Antimony. *Inorg. Chem.* **1967**, *6*, 1685−1692.
(16) Bottcher, P.; Doert, T.; Arnold, H.; Tamazyan, R. The Compounds with Layer Structures LnX_2. *Z. Kristallogr. - Cryst. Mater.* **2000**, *215*, 246−253.
(17) Aitken, J. A.; Cowen, J. A.; Kanatzidis, M. G. Metamagnetic Transition in $EuSe_2$: a New, Metastable Binary Rare-Earth Polychalcogenide. *Chem. Mater.* **1998**, *10*, 3928−3935.
(18) Ma, R.; Sasaki, T. Nanosheets of Oxides and Hydroxides: Ultimate 2D Charge-Bearing Functional Crystallites. *Adv. Mater.* **2010**, *22*, 5082−5104.
(19) Chhowalla, M.; Shin, H. S.; Eda, G.; Li, L.-J.; Loh, K. P.; Zhang, H. The Chemistry of Two-Dimensional Layered Transition Metal Dichalcogenide Nanosheets. *Nat. Chem.* **2013**, *5*, 263−275.
(20) Michioka, C.; Fukushima, K.; Suzuki, K.; Yoshimura, K. Physical Properties of RSe_{2-x} (R = Ce, Nd, Sm and Gd) and Rb_xGdSe_{3-y}. *J. Phys. Chem. Solids* **2005**, *66*, 1579−1582.
(21) Foran, B.; Lee, S.; Aronson, M. C. Commensurate and Incommensurate Lattice Distortions in Dysprosium Selenide ($DySe_{1.84}$) and Rubidium Dysprosium Selenide ($Rb_{0.33}DySe_{2.67}$). *Chem. Mater.* **1993**, *5*, 974−978.
(22) Doert, T.; Tsinde, B. P. F.; Lidin, S.; García, F. J. G. Site Occupancy Wave and Charge Density Wave in the Modulated Structure of $Nd_{0.6}Gd_{0.4}Se_{1.85}$. *J. Solid State Chem.* **2004**, *177*, 1598−1606.
(23) Doert, T.; Graf, C.; Vasilyeva, I. G.; Schnelle, W. Structural Frustration and Occupational Disorder: the Rare Earth Metal Polysulfides $Tb_8S_{14.8}$, $Dy_8S_{14.9}$, $Ho_8S_{14.9}$, and $Y_8S_{14.8}$. *Inorg. Chem.* **2012**, *51*, 282−289.
(24) Jung, M. H.; Alsmadi, A.; Kim, H. C.; Bang, Y.; Ahn, K. H.; Umeo, K.; Lacerda, A. H.; Nakotte, H.; Ri, H. C.; Takabatake, T. Superconductivity in Magnetically Ordered $CeTe_{1.82}$. *Phys. Rev. B: Condens. Matter Mater. Phys.* **2003**, *67*, 1892−1894.
(25) Webb, A. W.; Hall, H. T. High-Pressure Synthesis of Rare Earth Polyselenides. *Inorg. Chem.* **1970**, *9*, 843−847.
(26) Müller, C. J.; Doert, T.; Schwarz, U. High-Pressure Synthesis of Rare-Earth Metal Disulfidesand Diselenides LnX_2 (Ln= Sm, Gd, Tb, Dy, Ho, Er and Tm; X= S, Se). *Z. Kristallogr.* **2011**, *226*, 646−650.
(27) Zelenina, L. N.; Chusova, T. P.; Vasilyeva, I. G. Thermodynamic Investigation of the Phase Formation Processes in the Systems $LnSe_2$-$LnSe_{1.5}$ (Ln = La, Ce, Pr, Nd). *J. Chem. Thermodyn.* **2013**, *57*, 101−107.
(28) Chen, J.; Dorhout, P. K. Synthesis of Rare-Earth Polychalcogenides by Moderate Temperature Solid-State Metathesis. *J. Solid State Chem.* **1995**, *117*, 318−322.
(29) Creutz, S. E.; Fainblat, R.; Kim, Y.; De Siena, M. C.; Gamelin, D. R. A Selective Cation Exchange Strategy for the Synthesis of Colloidal Yb^{3+}-Doped Chalcogenide Nanocrystals with Strong Broadband Visible Absorption and Long-Lived Near-Infrared Emission. *J. Am. Chem. Soc.* **2017**, *139*, 11814−11824.
(30) Hendricks, M.; Campos, M.; Cleveland, G.; Jen-La Plante, I.; Owen, J. A Tunable Library of Substituted Thiourea Precursors to Metal Sulfide Nanocrystals. *Science* **2015**, *348*, 1226−1230.
(31) Campos, M. P.; Hendricks, M. P.; Beecher, A. N.; Walravens, W.; Swain, R. A.; Cleveland, G. T.; Hens, Z.; Sfeir, M. Y.; Owen, J. S. A Library of Selenourea Precursors to PbSe Nanocrystals with Size Distributions Near the Homogeneous Limit. *J. Am. Chem. Soc.* **2017**, *139*, 2296−2305.
(32) Gu, J.; Zhao, Z.-Q.; Ding, Y.; Chen, H.-L.; Zhang, Y.-W.; Yan, C. U.-H. Liquid-Phase Syntheses and Material Properties of Two-Dimensional Nanocrystals of Rare Earth-Selenium Compound Containing Planar Se Layers: $RESe_2$ Nanosheets and $RE_4O_4Se_3$ Nanoplates. *J. Am. Chem. Soc.* **2013**, *135*, 8363−8371.
(33) Wu, L.-M.; Sharma, R.; Seo, D.-K. Metathetical Conversion of Nd_2O_3 Nanoparticles Into NdS_2 Polysulfide Nanoparticles at Low Temperatures Using Boron Sulfides. *Inorg. Chem.* **2003**, *42*, 5798−5800.
(34) Kornienko, A.; Melman, J. H.; Hall, G.; Emge, T. J.; Brennan, J. G. Chalcogen Rich Lanthanide Clusters From Halide Starting Materials (II): Selenido Compounds. *Inorg. Chem.* **2002**, *41*, 121−126.
(35) Freedman, D.; Emge, T. J.; Brennan, J. G. Chalcogen-Rich Lanthanide Clusters: Compounds with Te^{2-}, $(TeTe)^{2-}$, TePh, TeTePh, $(TeTeTe(Ph)TeTe)^{5-}$, and $[(TeTe)_4TePh]^{9-}$ Ligands; Single Source Precursors to Solid-State Lanthanide Tellurides. *Inorg. Chem.* **2002**, *41*, 492−500.
(36) Lee, J.; Freedman, D.; Melman, J. H.; Brewer, M.; Sun, L.; Emge, T. J.; Long, F. H.; Brennan, J. G. Trivalent Lanthanide Chalcogenolates: $Ln(SePh)_3$, $Ln_2(EPh)_6$, $Ln_4(SPh)_{12}$, and $[Ln(EPh)_3]$ N(E = S, Se). How Metal, Chalcogen, and Solvent Influence Structure. *Inorg. Chem.* **1998**, *37*, 2512−2519.
(37) Regulacio, M. D.; Bussmann, K.; Lewis, B.; Stoll, S. L. Magnetic Properties of Lanthanide Chalcogenide Semiconducting Nanoparticles. *J. Am. Chem. Soc.* **2006**, *128*, 11173−11179.
(38) Hasegawa, Y.; Okada, Y.; Kataoka, T.; Sakata, T.; Mori, H.; Wada, Y. Synthesis and Photophysical Properties of EuS Nanoparticles From the Thermal Reduction of Novel Eu(III) Complex. *J. Phys. Chem. B* **2006**, *110*, 9008−9011.
(39) Mirkovic, T.; Hines, M. A.; Nair, P. S.; Scholes, G. D. Single-Source Precursor Route for the Synthesis of EuS Nanocrystals. *Chem. Mater.* **2005**, *17*, 3451−3456.
(40) Zhao, F.; Sun, H.-L.; Su, G.; Gao, S. Synthesis and Size-Dependent Magnetic Properties of Monodisperse EuS Nanocrystals. *Small* **2006**, *2*, 244−248.
(41) Burin, M. E.; Pushkarev, A. P.; Fukin, G. K.; Rumyantsev, R. V.; Konev, A. N.; Bochkarev, M. N. Synthesis of EuS and EuSe Particles via Thermal Decomposition of Dithio- and Diselenophosphinate Europium Complexes. *Nanotechnol. Russ.* **2017**, *12*, 66−72.
(42) Boncher, W. L.; Regulacio, M. D.; Stoll, S. L. Thermolysis of Lanthanide Dithiocarbamate Complexes. *J. Solid State Chem.* **2010**, *183*, 52−56.
(43) Zhang, X.; Qiao, X.-F.; Shi, W.; Wu, J.-B.; Jiang, D.-S.; Tan, P.-H. Phonon and Raman Scattering of Two-Dimensional Transition Metal Dichalcogenides From Monolayer, Multilayer to Bulk Material. *Chem. Soc. Rev.* **2015**, *44*, 2757−2785.
(44) Late, D. J.; Liu, B.; Matte, H. S. S. R.; Rao, C. N. R.; Dravid, V. P. Rapid Characterization of Ultrathin Layers of Chalcogenides on SiO2/Si Substrates. *Adv. Funct. Mater.* **2012**, *22*, 1894−1905.
(45) Jones, M. B.; Gaunt, A. J.; Gordon, J. C.; Kaltsoyannis, N.; Neu, M. P.; Scott, B. L. Uncovering F-Element Bonding Differences and

DOI: 10.1021/acs.chemmater.9b03067
Chem. Mater. 2019, 31, 7779−7789

Electronic Structure in a Series of 1:3 and 1:4 Complexes with a Diselenophosphinate Ligand. *Chem. Sci.* **2013**, *4*, 1189−15.
(46) Boland, K. S.; Hobart, D. E.; Kozimor, S. A.; MacInnes, M. M.; Scott, B. L. The Coordination Chemistry of Trivalent Lanthanides (Ce, Nd, Sm, Eu, Gd, Dy, Yb) with Diphenyldithiophosphinate Anions. *Polyhedron* **2014**, *67*, 540−548.
(47) Artem'ev, A. V.; Gusarova, N. K.; Malysheva, S. F.; Trofimov, B. A. Three-Component Reaction of Secondary Phosphines with Elemental Selenium and Amines. *Russ. J. Org. Chem.* **2010**, *46*, 592−593.
(48) Jones, M. B.; Gaunt, A. J.; Gordon, J. C.; Kaltsoyannis, N.; Neu, M. P.; Scott, B. L. Uncovering f-Element Bonding Differences and Electronic Structure in a Series of 1:3 and 1:4 Complexes with a Diselenophosphinate Ligand. *Chem. Sci.* **2013**, *4*, 1189−15.
(49) Müller, C. J.; Doert, T.; Schwarz, U. High-Pressure Synthesis of Rare-Earth Metal Disulfidesand Diselenides LnX_2 (Ln= Sm, Gd, Tb, Dy, Ho, Er and Tm; X= S, Se). *Z. Kristallogr.* **2011**, *226*, 646−650.
(50) Jorgens, S.; Mewis, A.; Hoffmann, R. D.; Pottgen, R.; Mosel, B. New Hexachalcogeno-Hypodiphosphates of Alkaline-Earth Metals and Europium. *Z. Anorg. Allg. Chem.* **2003**, *629*, 429−433.
(51) Maneeprakorn, W.; Nguyen, C. Q.; Malik, M. A.; O'Brien, P.; Raftery, J. Synthesis of the Nickel Selenophosphinates $[Ni(Se_2PR_2)_2]$ (R = iPr, tBu and Ph) and Their Use as Single Source Precursors for the Deposition of Nickel Phosphide or Nickel Selenide Nanoparticles. *Dalton Trans* **2009**, *17*, 2103−2106.
(52) Panneerselvam, A.; Nguyen, C.; Waters, J.; Malik, M.; O'Brien, P.; Raftery, J.; Helliwell, M. Ligand Influence on the Formation of P/Se Semiconductor Materials From Metal-Organic Complexes. *Dalton Trans* **2008**, 4499−4506.
(53) Maneeprakorn, W.; Malik, M. A.; O'Brien, P. The Preparation of Cobalt Phosphide and Cobalt Chalcogenide (CoX, X = S, Se) Nanoparticles From Single Source Precursors. *J. Mater. Chem.* **2010**, *20*, 2329−7.
(54) Shoko, E.; Smith, M. F.; McKenzie, R. H. Mixed Valency in Cerium Oxide Crystallographic Phases: Valence of Different Cerium Sites by the Bond Valence Method. *Phys. Rev. B: Condens. Matter Mater. Phys.* **2009**, *79*, 247−12.
(55) Evans, W. J. Advances in F Element Reductive Reactivity as a Paradigm for Expanding Lanthanide and Actinide Science and Technology. *J. Alloys Compd.* **2009**, *488*, 493−510.
(56) Lee, J.; Brewer, M.; Berardini, M.; Brennan, J. G. Trivalent Lanthanide Chalcogenolates: Synthesis, Structure, and Thermolysis Chemistry. *Inorg. Chem.* **1995**, *34*, 3215−3219.
(57) Nasilowski, M.; Mahler, B.; Lhuillier, E.; Ithurria, S.; Dubertret, B. Two-Dimensional Colloidal Nanocrystals. *Chem. Rev.* **2016**, *116*, 10934−10982.
(58) Hendricks, M. P.; Cossairt, B. M.; Owen, J. S. The Importance of Nanocrystal Precursor Conversion Kinetics: Mechanism of the Reaction Between Cadmium Carboxylate and Cadmium Bis-(Diphenyldithiophosphinate). *ACS Nano* **2012**, *6*, 10054−10062.
(59) Rhodes, J. M.; Jones, C. A.; Thal, L. B.; Macdonald, J. E. Phase-Controlled Colloidal Syntheses of Iron Sulfide Nanocrystals via Sulfur Precursor Reactivity and Direct Pyrite Precipitation. *Chem. Mater.* **2017**, *29*, 8521−8530.
(60) Tappan, B. A.; Barim, G.; Kwok, J. C.; Brutchey, R. L. Utilizing Diselenide Precursors Toward Rationally Controlled Synthesis of Metastable $CuInSe_2$ Nanocrystals. *Chem. Mater.* **2018**, *30*, 5704−5713.
(61) Chen, J.; Dorhout, P. Synthesis of Rare-Earth Polychalcogenides by Moderate Temperature Solid-State Metathesis. *J. Solid State Chem.* **1995**, *117*, 318−322.
(62) Dashjav, E.; Doert, T.; Bottcher, P.; Mattausch, H.; Oeckler, O. Crystal Structure of Samarium Selenide, SmSe1.90. *Z. Kristallogr. - New Cryst. Struct.* **2000**, *215*, 337−338.
(63) Yoo, D.; Kim, M.; Jeong, S.; Han, J.; Cheon, J. Chemical Synthetic Strategy for Single-Layer Transition-Metal Chalcogenides. *J. Am. Chem. Soc.* **2014**, *136*, 14670−14673.
(64) Vaughn, D. D., II; In, S.-I.; Schaak, R. E. A Precursor-Limited Nanoparticle Coalescence Pathway for Tuning the Thickness of Laterally-Uniform Colloidal Nanosheets: the Case of SnSe. *ACS Nano* **2011**, *5*, 8852−8860.
(65) Grzechnik, A.; Zheng, J. Z.; Wright, D.; Petuskey, W. T.; Mcmillan, P. F. $LaSe_{2-X}$ Compounds: Vibrational and Electrical Properties. *J. Phys. Chem. Solids* **1996**, *57*, 1625−1634.
(66) Bartsch, C.; Doert, T. Ternary Lanthanum Sulfide Selenides. -$LaS_{2-x}Se_x$ ($0 < X < 2$) with Mixed Dichalcogenide Anions X_2^{2-} (X = S, Se). *J. Solid State Chem.* **2012**, *185*, 101−106.
(67) Pinto, A. H.; Leite, E. R.; Longo, E.; de Camargo, E. R. Crystallization at Room Temperature From Amorphous to Trigonal Selenium as a Byproduct of the Synthesis of Water Dispersible Zinc Selenide. *Mater. Lett.* **2012**, *87*, 62−65.
(68) Wang, F.; Wang, X. Mechanisms in the Solution Growth of Free-Standing Two-Dimensional Inorganic Nanomaterials. *Nanoscale* **2014**, *6*, 6398−17.
(69) Meng, F.; Morin, S. A.; Forticaux, A.; Jin, S. Screw Dislocation Driven Growth of Nanomaterials. *Acc. Chem. Res.* **2013**, *46*, 1616−1626.
(70) Zhang, Q.; Liu, S.-J.; Yu, S.-H. Recent Advances in Oriented Attachment Growth and Synthesis of Functional Materials: Concept, Evidence, Mechanism, and Future. *J. Mater. Chem.* **2009**, *19*, 191−207.
(71) Wang, F.; Richards, V. N.; Shields, S. P.; Buhro, W. E. Kinetics and Mechanisms of Aggregative Nanocrystal Growth. *Chem. Mater.* **2014**, *26*, 5−21.
(72) Penn, L. R.; Banfield, J. Imperfect Oriented Attachment: Dislocation Generation in Defect-Free Nanocrystals. *Science* **1998**, *281*, 969−971.
(73) Yuwono, V. M.; Burrows, N. D.; Soltis, J. A.; Penn, R. L. Oriented Aggregation: Formation and Transformation of Mesocrystal Intermediates Revealed. *J. Am. Chem. Soc.* **2010**, *132*, 2163−2165.
(74) Zhang, X.; Lai, Z.; Ma, Q.; Zhang, H. Novel Structured Transition Metal Dichalcogenide Nanosheets. *Chem. Soc. Rev.* **2018**, *47*, 3301−3338.
(75) Dumcenco, D. O.; Kobayashi, H.; Liu, Z.; Huang, Y.-S.; Suenaga, K. Visualization and Quantification of Transition Metal Atomic Mixing in $Mo_{1-x}W_xS_2$ Single Layers. *Nat. Commun.* **2013**, *4*, 1351−1355.
(76) Tan, C.; Zhang, H. Two-Dimensional Transition Metal Dichalcogenide Nanosheet-Based Composites. *Chem. Soc. Rev.* **2015**, *44*, 2713−2731.
(77) Xu, C.; Peng, S.; Tan, C.; Ang, H.; Tan, H.; Zhang, H.; Yan, Q. Ultrathin S-Doped MoSe 2nanosheets for Efficient Hydrogen Evolution. *J. Mater. Chem. A* **2014**, *2*, 5597−5601.
(78) Dalafu, H. A.; Rosa, N.; James, D.; Asuigui, D. R. C.; McNamara, M.; Kawashima, A.; Omagari, S.; Nakanishi, T.; Hasegawa, Y.; Stoll, S. L. Solid-State and Nanoparticle Synthesis of EuS_xSe_{1-X} Solid Solutions. *Chem. Mater.* **2018**, *30*, 2954−2964.
(79) Ramasamy, K.; Sims, H.; Butler, W. H.; Gupta, A. Mono-, Few-, and Multiple Layers of Copper Antimony Sulfide ($CuSbS_2$): a Ternary Layered Sulfide. *J. Am. Chem. Soc.* **2014**, *136*, 1587−1598.
(80) Sasaki, S.; Driss, D.; Grange, E.; Mevellec, J.-Y.; Caldes, M. T.; Guillot-Deudon, C.; Cadars, S.; Corraze, B.; Janod, E.; Jobic, S.; et al. A Topochemical Approach to Synthesize Layered Materials Based on the Redox Reactivity of Anionic Chalcogen Dimers. *Angew. Chem., Int. Ed.* **2018**, *57*, 13618−13623.
(81) Cario, L.; Palvadeau, P.; Lafond, A.; Deudon, C.; Moëlo, Y.; Corraze, B.; Meerschaut, A. Mixed-Valence State of Europium in the Misfit Layer Compound $(EuS)_{1.173}NbS_2$. *Chem. Mater.* **2003**, *15*, 943−950.
(82) Radovsky, G.; Popovitz-Biro, R.; Stroppa, D. G.; Houben, L.; Tenne, R. Nanotubes From Chalcogenide Misfit Compounds: Sn-S and Nb-Pb-S. *Acc. Chem. Res.* **2014**, *47*, 406−416.
(83) Ellseev, A. A.; Laurier, J.; Kola, G.; Yarembash, E. I.; Suleimanov, M. Kh. An X-Ray Structure Study of Single Crystals of the Samarium Chalcogenides $SmSe_{2-X}$ and Sm_2S_3. *J. Struct. Chem.* **1968**, *9*, 464−465.

DOI: 10.1021/acs.chemmater.9b03067
Chem. Mater. 2019, 31, 7779−7789